Fibroblast alignment and matrix remodeling induced by a stiffness gradient in a skin-derived extracellular matrix hydrogel

Zhao, Fenghua; Zhang, Meng; Nizamoglu, Mehmet; Kaper, Hans; Brouwer, Linda A; Borghuis, Theo; Burgess, Janette K; Harmsen, Martin C; Sharma, Prashant K

Published in:
Acta Biomaterialia

DOI:
10.1016/j.actbio.2024.05.018

Publication date:
2024

Acta Biomaterialia 182 (2024) 67–80

Contents lists available at ScienceDirect

Acta Biomaterialia

journal homepage: www.elsevier.com/locate/actbio

Full length article

Fibroblast alignment and matrix remodeling induced by a stiffness gradient in a skin-derived extracellular matrix hydrogel

Fenghua Zhao[a,b,c], Meng Zhang[a,c], Mehmet Nizamoglu[c,d], Hans J. Kaper[a,b], Linda A. Brouwer[c], Theo Borghuis[c], Janette K. Burgess[a,c,d,1], Martin C. Harmsen[a,c,d,1], Prashant K. Sharma[a,b,1,*]

[a] University of Groningen, University Medical Centre Groningen, W.J. Kolff Institute for Biomedical Engineering and Materials Science-FB41, A. Deusinglaan 1, 9713 AV Groningen, the Netherlands
[b] University of Groningen, University Medical Centre Groningen, Department of Biomaterials and Biomedical Technology-FB40, A. Deusinglaan 1, 9713 AV Groningen, the Netherlands
[c] University of Groningen, University Medical Centre Groningen, Department of Pathology and Medical Biology, Hanzeplein 1 (EA11), 9713 GZ Groningen, the Netherlands
[d] University of Groningen, University Medical Centre Groningen, Groningen Research Institute for Asthma and COPD (GRIAC), Hanzeplein 1 (EA11), 9713 AV Groningen, the Netherlands

ARTICLE INFO

Article history:
Received 25 January 2024
Revised 17 April 2024
Accepted 6 May 2024
Available online 13 May 2024

Keywords:
Gradient stiffness
Extracellular matrix hydrogel
Fibroblasts
Collagen
Scarring

ABSTRACT

Large skin injuries heal as scars. Stiffness gradually increases from normal skin to scar tissue (20x higher), due to excessive deposition and crosslinking of extracellular matrix (ECM) mostly produced by (myo)fibroblasts. Using a custom mold, skin-derived ECM hydrogels (dECM) were UV crosslinked after diffusion of ruthenium (Ru) to produce a Ru-dECM gradient hydrogel. The Ru diffusion gradient equates to a stiffness gradient and models physiology of the scarred skin. Crosslinking in Ru-dECM hydrogels results in a 23-fold increase in stiffness from a stiffness similar to that of normal skin. Collagen fiber density increases in a stiffness-dependent fashion while stress relaxation also alters, with one additional Maxwell element necessary for characterizing Ru-dECM. Alignment of fibroblasts encapsulated in hydrogels suggests that the stiffness gradient directs fibroblasts to orientate at ~45 ° in regions below 120 kPa. In areas above 120 kPa, fibroblasts decrease the stiffness prior to adjusting their orientation. Furthermore, fibroblasts remodel their surrounding ECM in a gradient-dependent fashion, with rearrangement of cell-surrounding ECM in high-stiffness areas, and formation of interlaced collagen bundles in low-stiffness areas. Overall, this study shows that fibroblasts remodel their local environment to generate an optimal ECM mechanical and topographical environment.

Statement of significance

This study developed a versatile *in vitro* model with a gradient stiffness using skin-derived ECM hydrogel with unchanged biochemical environment. Using Ruthenium crosslinking, a 20-fold stiffness increase was achieved as observed in fibrotic skin.

The interaction between fibroblasts and matrix depends on changes in the matrix stiffness. The stiffness gradient directed the alignment of fibroblasts with ~45° in regions with≤ 120 kPa. The cells in regions with the higher stiffness decreased stiffness first and then oriented themselves. Furthermore, fibroblasts remodeled surrounding ECM and regulated its mechanics in a gradient-dependent fashion to reach an optimal condition.

Our study highlights the dynamic interplay between cells and surrounding matrix, shedding light on potential mechanisms and strategies to target scar formation and remodeling.

* Corresponding author at: University Medical Center Groningen, Department of Biomaterials and Biomedical Technology, Deusinglaan 1, 9713 AV Groningen, the Netherlands.
E-mail address: p.k.sharma@umcg.nl (P.K. Sharma).
[1] These authors contributed equally.

https://doi.org/10.1016/j.actbio.2024.05.018
1742-7061/

1. Introduction

The skin is the largest organ of the human body. Appropriate healing of the skin after injury is necessary to restore the barrier function [1,2]. Dermal wound healing is a spatio-temporally regulated process. It involves four defined and overlapping stages: coagulation, inflammation, proliferation, and remodeling/fibrosis [3-5]. However, if not properly regulated, accumulation of extracellular matrix (ECM) and tissue stiffening during the last stage of wound healing can lead to pathological dermal scarring [6]. The pivotal cells involved in fibrosis are fibroblasts and their differentiated form - myofibroblasts, as these remodel ECM [7,8]. Numerous fibroblasts migrate to the injured area and produce collagens to replace the fibrin clot formed during the coagulation phase of the wound healing process. During the remodeling phase, fibroblasts are activated and differentiate into myofibroblasts [9]. These myofibroblasts express more α-smooth muscle actin than fibroblasts and are contractile, as well as migratory [10]. They act as natural stitches to keep wounds closed, which they then fill with ECM components such as collagens. The wound then enters the final stage of remodeling. During the remodeling process, various factors, such as hypoxia in the wound, continued inflammatory stimulation, excessive wound tension, can lead to continued deposition and disordered arrangement of collagens. Finally, if the wound healing becomes dysregulated, the deposited collagen is heavily crosslinked by the persistent and chronically activated myofibroblasts to form fibrosis, rather than undergoing apoptosis at the time when the tissue structural integrity is restored [11,12].

An important element of skin fibrosis is the gradient of stiffness in the ECM that extends from the healthy dermis into the scar [13-15]. In fact, stiffness gradients also occur in other pathological conditions *in vivo* such as fibrosis of liver, heart, lungs and kidney [16-19]. Furthermore, because the ECM provides attachment sites for cell adhesion receptors, changes in the biophysical tissue microenvironment directly influences the behavior and function of fibroblasts and may dictate phenotypic changes e.g. to myofibroblasts [20]. The mechanics of ECM affect the cytoskeleton, matrix adhesion, cell proliferation and differentiation of fibroblasts cultured in two-dimensions (2D) [21-25]. As cells naturally exist in complex three-dimensional (3D) ECM networks [26], current studies shift towards 3D culturing to better understand how matrix mechanical properties affect cell phenotype [27]. Dermal fibroblasts in 3D culture in matrices of different stiffnesses showed that, unlike cells that expand more with increasing 2D stiffness, high stiffness in 3D causes cells to round up and change towards a pro-inflammatory, pro-remodeling state [28-30]. Most of these *in vitro* studies apply uniform stiffness substrates, in which the gradient of stiffness changes of tissue ECM *in vivo* is not replicated. Such uniform stiffness substrates limit potential studies on how fibroblasts are influenced by diverse biophysical environments *in vivo*. In addition, the widely used hydrogels, whether natural hydrogels such as collagen, hyaluronic acid, chitosan, or synthetic hydrogels such as polyvinyl alcohol (PVA) and polyacrylic acid (PAA), do not sufficiently approximate the complex natural biochemical environment for interrogating cell responses, either in composition or structure [31-35].

To address this challenge, we established an *in vitro* scar model with stiffness gradients using skin-derived decellularized ECM (dECM) hydrogel. These dECM hydrogels comprise the natural ECM components and mimic the physiological environment of (scarred) skin. This experimental system builds on our previous study in which we developed a non-cytotoxic method to uniformly modulate the stiffness of lung-derived dECM hydrogel by introducing visible UV (UV/vis) - induced ruthenium (Ru)/sodium persulfate (SPS) crosslinking [36]. In the presence of visible light and a cross-linker electron acceptor SPS, Ru^{2+} is photolytically oxidized to Ru^{3+}. The presence of Ru^{3+} can oxidize aromatic residues such as in tyrosine residues in proteins. The free tyrosyl radical then reacts with another free tyrosyl radical to form a covalent dityrosine bond i.e. crosslinking neighboring protein chains. dECM hydrogels cross-linked with Ru not only have increased stiffness levels, but also have increased higher density matrix percentages and smaller average fiber lengths. In the current study, we introduced Ru crosslinking into skin-derived dECM to generate the stiffness gradient hydrogels. We investigated the physical characteristics of these gradients and their influence on fibroblasts in particular pertaining to ECM remodeling.

2. Experimental methods

2.1. Decellularization of porcine skin tissue

Porcine skin tissue was obtained from a local abattoir (Kroon Vlees, Groningen, the Netherlands). The epidermis and subcutaneous fat were removed. Then the remaining dermal tissue was cut into ~ 3 mm x 3 mm x 3 mm cubes which were homogenized in a kitchen blender (Bourgini, Breda, The Netherlands) until a paste was formed, while keeping the temperature below 37 °C. The homogenized skin was decellularized as we described previously (Fig. 1A) [37,38]. Briefly, the minced tissue was washed with Dulbecco's phosphate-buffered saline (DPBS) and then sonicated for 1 min at 100 % power. Next, 0.05 % trypsin (Thermo Fisher Scientific, US) dissolved in DPBS was used to digest the tissue slurry, followed by deep digestion using subsequent incubations in saturated 6 M NaCl solution, 1 % sodium dodecyl sulfate (SDS) (Sigma-Aldrich, US), 1 % Triton X-100 (Sigma-Aldrich, US) and 1 % sodium deoxycholate (Sigma-Aldrich, US), which were all dissolved in distilled water and each added to the tissue slurry for 24 h incubations at 37 °C with shaking. Washing 3 times with distilled water after each step was undertaken to remove residual digestive. The volume of solution at each step was 5-fold more than the tissue volume. Next, residual DNA was digested with 30 µg/mL DNase (Sigma-Aldrich, US) in 10 mM Tris–HCl buffer with pH 8, 1.3 mM $MgSO_4$ (Sigma-Aldrich, US) and 2 mM $CaCl_2$ (Sigma-Aldrich, US) for 24 h at 37 °C with shaking. Then, three volumes of 70 % ethanol were used to sterilize the decellularized ECM (dECM) tissue overnight with shaking. At the end, dECM tissue was frozen in liquid nitrogen and lyophilized with a FreeZone Plus lyophilizer (Labconco, US). The Ultra-Turrax (IKEA, Germany) with liquid nitrogen crushed the lyophilized dECM tissue into a fine powder which was stored in an airtight plastic bottle at −20 °C.

2.2. Preparation of dECM pre-gel

The dECM (20 mg/mL) powder was added to 0.01 M hydrochloric acid (HCl) with 2 mg/mL pepsin and digested in a sterile glass vial while mixing using a magnetic stirring bar at 500 rpm at room temperature for 24 h. The homogeneously dissolved ECM solution was neutralized by adjusting it to pH 7.4 with 0.1 M NaOH to stop the digestion and then adjusted to 1x PBS by adding one-tenth volume 10x PBS. This so-called dECM pre-gel was stored at 4 °C.

2.3. Making gradient stiffness skin dECM hydrogels

A polylactic acid (PLA) front-mold, designed to enable the generation of our gradient hydrogel, was printed using a 3D printer (ULT216931, Ultimaker S3, Netherlands) (Fig. 1B) (See printing script in Suppl. materials). Liquid polydimethylsiloxane (PDMS, Sylgard 184, Dow Corning, Netherlands) composed of the elastomer and the cross-linker in a 10:1 ratio by weight, was then poured into the PLA mold, until it completely filled it. A microscope slide (25 mm x 76 mm, Thermo Fisher Scientific, US) was placed on

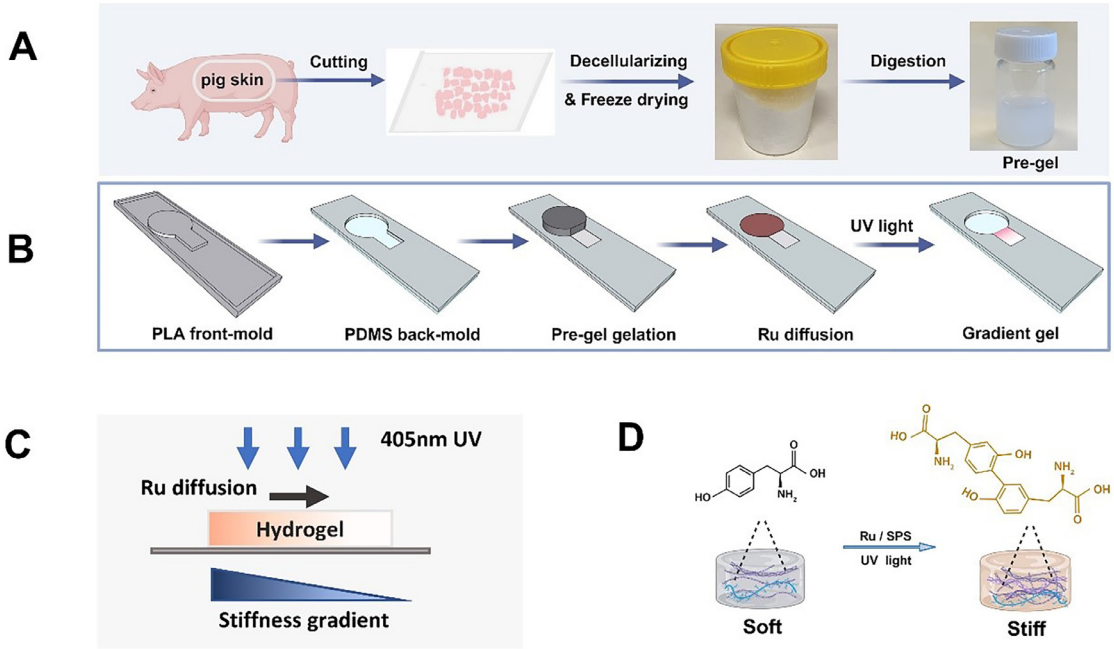

Fig. 1. Schematic outlining the steps in designing and creating a gradient stiffness hydrogel. A) Porcine skin decellularization and ECM (dECM) pre-gel preparation. Porcine skin was blended, decellularized, freeze-dried and ground to a fine powder. Afterwards, the ECM powder was pepsin digested to prepare the pre-gel solution. B) Polydimethylsiloxane (PDMS) mold fabrication to enable gradient stiffness dECM hydrogel generation. Polylactic acid (PLA) pre-mold was first three dimensionally (3D) printed, and liquid PDMS was poured into the PLA mold which was subsequently covered by a glass microscope slide and incubated overnight to allow the development of a tight connection between the PDMS mold and the glass. This PDMS mold contained a cylindrical space connected to a cuboidal space. The dECM pre-gel solutions were poured into the cuboid space while blocking the cylindrical space with a plug (shown in dark grey color). After the thermal gelation of the pre-gel, the plug was removed and a Ru crosslinking solution (shown in red color) was poured and incubated for 3 h to allow for diffusion of ruthenium (Ru) and sodium persulfate (SPS) into the gel, followed by UV/vis crosslinking. C) A schematic diagram of introducing Ru crosslinks in the hydrogel to create the stiffness-gradient hydrogel. D) A schematic of the chemical change induced during the visible UV light activated dityrosine synthesis using the Ruthenium kit for the ECM crosslinking: Ruthenium catalyses the formation of dityrosine dimers between protein chains. Figure created with BioRender.

top of the mold and the solution was cured at 50 °C overnight. Then, the cast PDMS back-mold with the tightly adhered microscope slide was separated from the PLA front-mold (See Figure S1 for details). The PDMS back-mold contained a cuboidal space of 10 mm x 8 mm x 1.5 mm (120 mm^3) connected to a cylindrical space of radius 19 mm and height 1.5 mm (425 mm^3). The cylindrical to cuboidal volume ratio was 3.5.

The cylindrical space was first filled by placing a plug with a thin layer of parafilm, before the dECM pre-gel was poured into the cuboidal space. The dECM pre-gel filled PDMS mold was incubated at 37 °C for 1 hour to allow for thermal gelation. The plug was carefully removed from the cylindrical space and the cross-linker solution was poured into this space (Fig. 1B). The cross-linker solution was prepared using a ruthenium visible light photo initiator (400–450 nm) kit (Advanced BioMatrix, US) containing pentamethyl cyclopentadienyl bis(triphenylphosphine) ruthenium (II) chloride (CAS Number: 92361-49-4, hereafter referred as ruthenium (Ru)) and sodium persulfate (SPS, CAS: 7775–27–1). A series of ruthenium concentrations (0, 1.5 mM, 3 mM, 6 mM, and 15 mM coupled with 30 mM sodium persulfate in sterile DPBS were prepared and added to the cylindrical space of the mold. Then the mold was placed in a cell incubator at 37 °C for 3 h, to allow for lateral diffusion of ruthenium and sodium persulfate into the gel to generate a concentration gradient. After 3 h the cross-linker solution was removed from the mold reservoir and the hydrogel with ruthenium gradient was photo crosslinked by placing at a 4.5 cm distance from two 9 W lamps emitting UV A light at 405 nm for 5 min (UV/vis light density: 20 mW/cm^2) (Fig. 1C). Under the UV/vis exposure, ruthenium catalyzed the covalent bond formation of di-tyrosine dimers between protein chains in dECM hydrogel (Fig. 1D). The hydrogels (10mm×8mm×1.5 mm) with stiffness gradient (Fig. 1C) were labeled as Ru0-dECM, Ru1.5-dECM, Ru3-dECM, Ru6-dECM, and Ru15-dECM, respectively. The hydrogels were then incubated in 6 mL DPBS for 4 h at 37 °C to keep them moist before testing the mechanical properties. After our initial validation experiments, we selected ruthenium/sodium persulfate of 3 mM Ru/30 mM SPS (Ru3-dECM) as the final concentration for all subsequent experiments (referred to as Ru-dECM), the control gel (dECM hydrogel) was then prepared by adding the same volume and concentration of cross-linker solution without UV/vis light exposure.

2.4. Mechanical properties

2.4.1. Micro low-load compression tester measurements

The stiffnesses of dECM and Ru-dECM hydrogels were assessed by using a micro low-load compression tester (μLLCT, UMCG, Groningen, The Netherlands) at room temperature. The μLLCT performed micron-scale multi-point automatic testing on hydrogels, which was helpful to determine stiffness gradients at multiple areas along the hydrogel. The μLLCT consists of a micro force sensing probe FT-S1000 (Femto Tools, Switzerland) with a 50×50 μm square tip area mounted on a precision linear stage Q522.230 (PI, Karlsruhe, Germany) and a bottom plate which can be moved on the x and y axes (Fig. 2A). Data acquisition and stage control were carried out using a program written in MATLAB software (MathWorks® Inc., Natick, US). The μLLCT probe tip was slowly brought in contact with the hydrogel and hydrogel compressed to measure the stiffness of the hydrogel. Hydrogel properties were determined at 15 discrete and equidistant points spread over 9 mm along the length of the gradient hydrogel between the high Ru concentration end to low Ru concentration end. At each testing point the hydrogel was compressed to 90 % of its original thickness (imposed

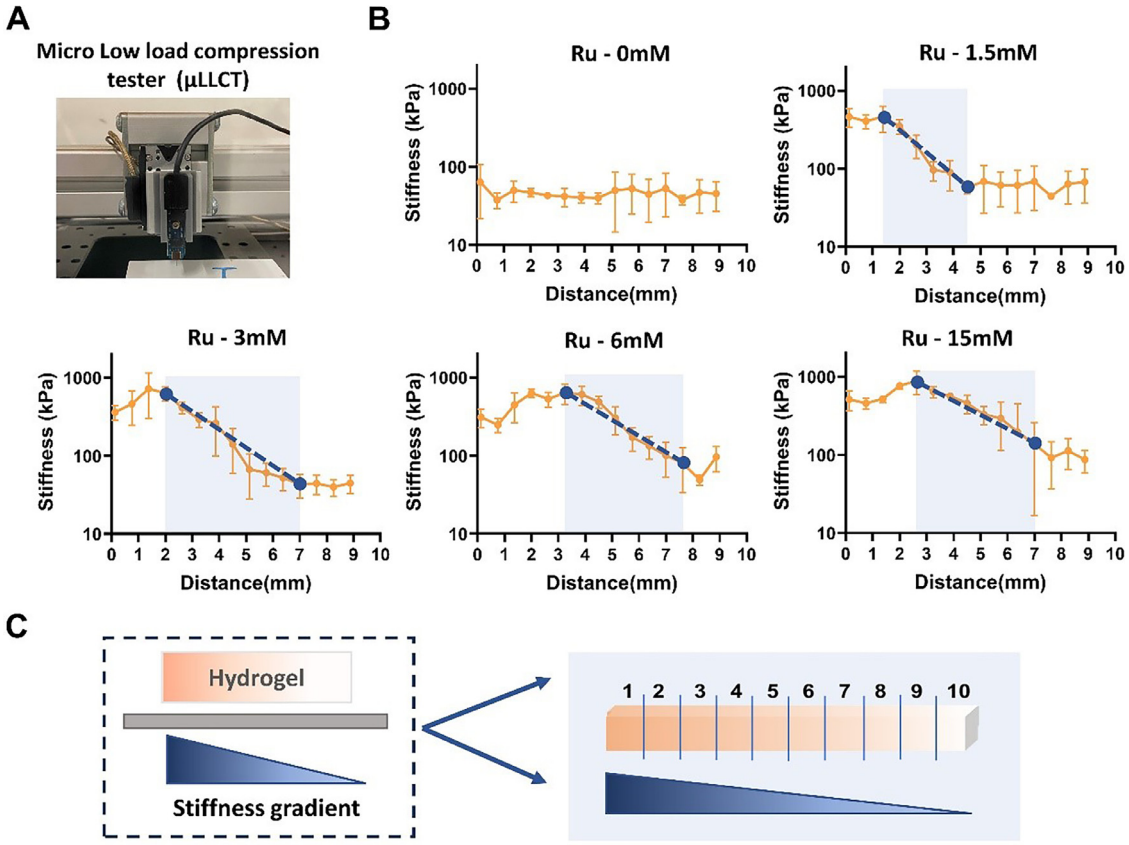

Fig. 2. Stiffness of dECM hydrogel after the diffusion of a series of initial Ru concentrations and UV/vis crosslinking. A) Micro low-load compression tester (μLLCT) used for measuring stiffness in compression mode. Using MATLAB software, the system automatically captured the stress-strain curve (the slope is the Young's modulus indicative of stiffness) at 15 points spread over a 9 mm distance in the horizontal direction from high Ru concentration end to low Ru concentration end. B) Stiffness gradients of Ru-dECM hydrogels for different initial Ru concentration. Each dot represents the mean ± standard deviation generated from measurement on five independent experiments ($n = 5$). The grey box length represents the span of the stiffness gradient; the blue dashed line represents the slope of the stiffness gradient. C) A schematic for dividing the entire stiffness gradient of Ru-dECM hydrogel into 10 zones for all the subsequent analyses.

strain, ε of 0.1) at a deformation speed of 10 %/s (strain rate, $\dot{\varepsilon}$ of 0.1s^{-1}) and kept compressed for 5 s. The probe was then elevated 300 μm and moved to next testing position until all 15 points were tested. During the initial 1 second compression step, the applied force, F, was converted to stress, σ, by dividing F by the area of cross-section, A, of the probe tip ($A = 2500$ μm^2). The deformation was converted into strain, ε, by dividing the compression depth by the original thickness of the hydrogel. Stress was plotted as a function of strain and the slope of the linear fit was taken as the Young's modulus in Pascals (Pa or N/m^2), which was indicative of the hydrogel stiffness at that testing point and a strain rate ($\dot{\varepsilon}$) of 0.1 s^{-1}.

2.4.2. Low-load compression tester measurements

The viscoelastic properties (stiffness, stress relaxation) of the gradient hydrogels, were tested using the low-load compression tester (LLCT, Mytri Aeldoom, the Netherland) fitted with a 0.5 mm diameter probe. LabVIEW 7.2 program (National Instruments, Austin, US) was used for the LLCT load cell and linear positioning for control and data acquisition. The LLCT probe was used to compress the hydrogel to 80 % of its original thickness at a deformation rate of 20 % s^{-1} (Strain rate, $\dot{\varepsilon} = 0.2$ s^{-1}). As with the μLLCT, the slope of the linear part of the stress-strain curve was taken as the Young's modulus (Pa or N/m^2), which was indicative of the stiffness of the hydrogel. After compression, a constant strain of 20 % was maintained for 50 s. The required stress to maintain the same degree of compression continuously decreased with time ($\sigma(t)$) due to the viscoelastic nature of the hydrogel, which represented the stress relaxation. The stress ($\sigma(t)$) was converted into relaxing stiffness ($E(t)$) by dividing with the constant strain of 0.2. A Maxwell function i.e., Eq. (1) was fitted to $E(t)$ to get the values of E_i and τ_i for individual Maxwell elements. The τ_i was the relaxation time constant for each individual Maxwell element. Eq. (2) was used to represent relative importance (R_i) for each Maxwell element (ME) parallelly placed in the generalized Maxwell model. For natural materials, multiple MEs are necessary to explain the experimentally observed stress relaxation behavior. The minimum number of MEs (n) necessary to explain the stress relaxation behavior of a measured hydrogel was determined by monitoring the decrease in chi-square function expressed by Eq. (3) over N measurement points. When no further decrease in chi-square function was observed, then that number (n) was used as the minimum number of MEs required to explain the stress relaxation behavior. In general, for replicate measurements the same minimum number of MEs were found to be necessary.

$$E(t) = E_1 e^{t/\tau_1} + E_2 e^{t/\tau_2} + E_3 e^{t/\tau_3} + \ldots + E_n e^{t/\tau_n} \quad (1)$$

$$R_i = E_i/(E_1 + E_2 + E_3 + \cdots + E_n) \quad (2)$$

$$\chi^2 = \sum_{j=0}^{N} \left[\frac{E_j - E(t_j)}{\sigma_j} \right] \quad (3)$$

2.5. 3D cell culture

Primary human dermal neonatal fibroblasts (HDFn, PCS-201–010™, ATCC, US) ($n = 5$) were cultured in growth media composed of high glucose (25 mM) Dulbecco's Modified Eagle's Medium (DMEM, Lonza, Switzerland), 10 % fetal bovine serum (FBS, Gibco, Germany), 1 % glutamine (BioWhittaker®, Verviers, Belgium) and 1 % penicillin/streptomycin (Gibco, Paisley, UK). Upon reaching 90 % confluency, the cells were harvested using 0.25 % Trypsin-EDTA (Gibco, US) in DPBS and then the cell numbers were counted using a NucleoCounter NC-200 TM (Chemometec, Allerod, Denmark). Next, the cells were collected through centrifuging at 500 x g and resuspended in 50 µL growth media. The resuspended cells were mixed gently with the dECM pre-gel at a density of 1.7×10^6 cells/mL. Next, the mold was inserted into a well of a 4-well rectangular dish (Thermo Scientific™ 167063, US; Figure S5). The mixtures of cells and pre-gel were cast into the cuboid space of the mold (Fig. 1B) while the connected cylinder groove part was completely closed off with a plug. After the mixtures of cells and pre-gel incubated at 37 °C for one hour to allow complete thermal gelation, the plug in the cylinder groove was removed and replaced with cross-linking solution (DPBS with 3 mM Ru and 30 mM SPS). Next, the mold was incubated at 37 °C for 3 h, to allow the Ru and SPS to diffuse into the gel generating the stiffness gradient after photo crosslinking at 405 nm for 5 min. The control cell encapsulated dECM hydrogels were obtained without crosslinking. Following this 7 mL of growth media was added to each well and the gels were then placed into a cell culture incubator.

2.6. Live-Dead staining

Cell viability and morphology were determined by staining live cells, dead cells, and cell nuclei using Calcein AM (C1430- Thermo Fisher Scientific, US), propidium iodide (PI; P4170, Sigma Aldrich, US) and Hoechst (Hoechst 33342, Thermo Fisher Scientific, US) dyes respectively. After culturing for 4 h, 1 d and 5 d, the hydrogels were removed from the mold and washed three times with DPBS and then incubated with staining solution (5 µM Calcein AM, 3 µM PI in DPBS, 8 µM Hoechst). From this step onwards, aluminum foil was used to protect the hydrogel from light. After incubating for 30 min at 37 °C, the samples were washed twice with DPBS to remove excess staining solution, and then serum-free medium was added to maintain cell viability. Finally, the hydrogels were transferred to a 35 mm glass bottom dish (Thermo Scientific™, C150680, UK) and imaged within 2 h using a Zeiss Cell Discoverer 7 imaging system (Zeiss, Jena, Germany) with GFP (509 nm) and Texas Red (615 nm), DAPI (405 nm) channels. The cell orientation in both Ru-dECM and dECM gel was characterized using Fiji with orientation J macro [39]. Cell morphology in both Ru-dECM and dECM hydrogels was analyzed based on Calcein AM stained of living fibroblasts: average spreading area of HDFn fibroblasts was evaluated using Fiji; cell aspect ratio was calculated using the plug-in PAT-GEOM [40] in Fiji.

2.7. Hydrogel ultrastructure analyses using scanning electron microscopy

Hydrogel ultrastructure was investigated using scanning electron microscopy (SEM). After Ru crosslinking of the skin dECM pre-gel, the cell-free Ru-dECM and dECM hydrogels were fixed with 2.5 % glutaraldehyde (111–30–8, Sigma, Darmstadt, Germany) and 2 % paraformaldehyde (PFA; Sigma-Aldrich) in PBS at 4 °C overnight. After fixation, 2 % agarose (Invitrogen, US) in DPBS was used to pre-embed hydrogels to avoid shrinkage of the hydrogel during dehydration. Next, the hydrogels were stepwise dehydrated through a graded ethanol series before embedding them in paraffin. Then, the paraffin-embedded hydrogels were cut into 50 µm thick sections which were mounted onto glass coverslips (size 18 × 18 mm, Merk, Catalog #BR470045). After drying, the sections were deparaffinized in xylene and rehydrated in a series of 100 %, 96 %, and 70 % ethanol. Dry sections were glued on top of 6 mm SEM pin stubs (Agar Scientific, Stansted, UK) and carbon coated using a Leica EM ACE600 sputter coater device (Leica Microsystems B.V., Amsterdam, Netherlands). Hydrogels were visualized at 25,000× magnification, at 3 kV with a Zeiss Supra 55 STEM (Carl Zeiss NTS GmbH). The analyses were performed from images of three independent hydrogels using Fiji with the plugin DiameterJ [41].

2.8. Histological characterization of ECM protein fiber structure

After 4 h, 1 d, and 5 d cell culture, hydrogels were fixed in 2 % PFA in DPBS overnight. Then, the samples were pre-embedded/dehydrated/paraffin embedded as described above in Section 2.7. The paraffin-embedded hydrogels were cut into 4 µm thin sections. The sections were deparaffinized and stained with Hoechst (8 µM in DPBS) for 15 min followed by 0.1 % picrosirius red (PSR; Sigma-Aldrich) in 1.3 % aqueous solution of picric acid (Sigma-Aldrich) to visualize the cell nuclei and collagen fibers respectively. After washing with 3 changes of dH_2O and 3 changes of 0.5 % acetic acid, the sections were mounted with 0.7 % acetic acid in glycerol. The slides were stored at 4 °C, in the dark, before they were imaged.

2.9. Immunofluorescence staining

Before immunofluorescent staining, the 4 µm deparaffinized sections were heated in 10 mM citrate buffer pH 6 at 85 °C for 4 h for antigen retrieval. Then sections were incubated in 0.3 % hydrogen peroxide (H_2O_2, Merck, Germany) for 30 min to block endogenous peroxidase activity. After 3 times washing with Tris Buffered Saline buffer (TBS, Thermo Fisher Scientific), the sections were blocked with 4 % bovine serum albumin (BSA) in TBS for 15 min and subsequently incubated at room temperature for 2 h with the primary antibody Ki67 (ab16667, Abcam, rabbit anti-human, 1:200) for detecting cell proliferation. After 3 times washing with TBS, the peroxidase-conjugated goat-anti-rabbit secondary antibody (Thermo Fisher Scientific, catalog #A32731, 1:200) was added for one hour at room temperature, followed by color development by incubation with the Opal 570 (Akoya Biosciences, Marlborough MA, US, 1:200) diluted in 0.1 M borate buffer with 0.003 % hydrogen peroxide (Merck, Darmstadt, Germany). Finally, the sections were treated with DAPI (Thermo fisher scientific, Lot:2328978, US) (1:5000) in DPBS for 30 min. The sections were mounted using Citifluor mounting medium (Science Services, Munich, Germany) and stored at 4° in the dark before acquiring images.

2.10. Section imaging and image analyzing

The cell live-dead staining images were obtained by scans using the Zeiss Cell discoverer 7 imaging system as described above. The fluorescent images of stained PSR and Hoechst sections were generated with the fluorescence slide scanner Olympus VS200(Olympus Corporation, Japan) at 40x magnification using λ_{ex} 561 nm / λ_{em} 670 nm for PSR and λ_{ex} 405 nm / λ_{em} 455 nm for Hoechst. The intensity of PSR-stained collagen fibers was analyzed with Fiji [42]. Fluorescent images of Ki67 and DAPI staining were generated with a Leica SP8 X laser confocal microscope (Leica, Wetzlar, Germany) using λ_{ex} 561 nm / λ_{ex} 617 nm and λ_{ex} 405 nm / λ_{em} 455 nm at 40 x magnification. CellProfiler 4.2.1 software was used to quantify the percentage of Ki67 positive fibroblasts [43].

2.11. Statistical analyses

All statistical analyses were performed using GraphPad Prism v9.2.0 (GraphPad Company, San Diego, CA, US). All data are shown as mean ± standard deviation from the experiments that were performed with least five independent experiments. The figure legends indicate the sample size associated with each experiment. Normality of the data was tested with a QQ plot and a Shapiro-Wilk test [44]. When normality was confirmed, a one-way or two-way analysis of variance (ANOVA) was employed for data analysis. When data were not normally distributed, Mann-Whitney test and Kruskal-Wallis test were used for data analyses. All data were considered significantly different at $p < 0.05$.

3. Results

3.1. Characterizations of the stiffness gradient of Ru-dECM hydrogel under variable Ru working concentrations

In the custom mold, controlled by Fick's laws of diffusion, Ru naturally diffused from one end of the hydrogel to the other due to the concentration differences. The flow rate of a substance (i.e., the amount of substance passing through a unit area per unit time) is linearly related to the concentration gradient. This resulted in the generation of a gradient in Ru concentration along the hydrogel over time. Since the rate of the cross-linking reaction depends on the concentration of Ru present at any location within the hydrogel, the degree of cross-linking of the hydrogel also exhibited a gradient distribution. As a result, control dECM hydrogels (Ru: 0 mM) had a consistent (low) stiffness throughout the entire gel, while all four gels with Ru concentrations (Ru: 1.5, 3, 6, 15 mM) yielded stiffness gradients which extended to the stiffness seen in the control at their far end (Fig. 2B), as measured by μLLCT. The main differences of these gradients were the inclines of the curves. The gradient induced by 1.5 mM Ru extended over a distance of 3.1 mm and had a slope of −130.3 kPa/mm. In contrast, the gradient induced by 3 mM Ru extended over a distance of 5 mm with a slope of −118.4 kPa/mm, while the gradient induced by 6 mM Ru and 15 mM Ru extended over a distance of 3.8 mm with a slope of −38.7 kPa/mm and 4.4 mm with −120.5 kPa/mm. Because 3 mM Ru yielded the widest gradient, this was selected for further experiments, referred to from here on as Ru-dECM. Subsequently, the stiffness gradient region of Ru-dECM spanning from 2 mm to 7 mm was selected as the focus of our research and divided into 10 equal-distant zones of 0.5 mm each (Fig. 2C). For high accuracy, a μLLCT with 50×50 μm square probe was used here to identify the stiffness gradients. However, this procedure was time-consuming and μLLCT had limited ability to detect stress relaxation. Therefore, in subsequent viscoelasticity testing of hydrogels LLCT was performed with a 0.5 mm diameter round probe. Due to differences in probe size, the stiffness values obtained with μLLCT differed slightly from LLCT values, yet the shape of the stiffness curves was retained.

3.2. Regulation of viscoelastic mechanical properties of cell-free dECM hydrogels by Ru-introduced crosslinking

First, without encapsulating cells, the effect of Ru-introduced crosslinking on the mechanical properties of dECM hydrogels was explored. The stiffness of cell-free Ru-dECM under the LLCT test ranged from 459 ± 92 kPa to 20 ± 7 kPa over 5 mm and dECM hydrogel stiffness remained constant at 8 ± 2 kPa (Fig. 3A). To compare the effects of hydrogels with different stiffness values on subsequent encapsulating of cells, zones 2, 5, and 8 were selected to represent high, medium, and low stiffness zones of the gradient. This yielded stiffness values for zone 2: 349 kPa, zone 5: 107 kPa, and for zone 8: 32 kPa. Stress relaxation curves for cell-free Ru-dECM and dECM hydrogels at 4 h under constant deformation in 50 s showed a relaxation of over 93.2 % in both hydrogels in all zones (Fig. 3B). The time to reach 50 % stress relaxation also did not differ between Ru-dECM and dECM hydrogels and was less than 1 s (Fig. 3C). Mathematical fitting of the relaxation curves with the generalized Maxwell model, yielded three elements for control dECM hydrogels and four elements for crosslinked hydrogels (Fig. 3D). Each Maxwell element was characterized by a relaxation time constant (τ) and its relative importance (R_i). The τ values are presented in Table 1, and the R_i values are plotted in Fig. 3D. At 4 h post-crosslinking, the shortest ME1 ($\tau \sim 0.2$ s, Table 1) had the largest relative contribution irrespective of crosslinking. ME1 contributed approximately 65 % of the relaxation curve in dECM hydrogels while it accounted for 45–55 % in Ru-dECM hydrogels. In cell-free Ru-dECM, the contributions of the ME2, ME3 and ME4 decreased successively, while ME2 and ME3 contributed equally (∼20 % each) for dECM hydrogels. The relaxation time constants (τ) of these four MEs in gradient stiffness hydrogels were 0.2 s, 1.3 s, 6.6 s, and 71 s (Table 1), respectively. The relaxation constant (τ) of each element was unaffected by the hydrogel stiffness (i.e. it remained the same in zone 2, zone 5 and zone 8). The τ of the three MEs in dECM hydrogels were 0.2 s, 2.1 s, and 16 s (Table 1), respectively. From the analysis of the time constants, the additional ME (ME4) needed to explain the relaxation in Ru-dECM corresponded to the relaxation time constant of 71 s.

3.3. Regulation of hydrogel mechanical properties by encapsulated HDFn cells

Upon 3D encapsulation of HDFn cells in the hydrogels (4 h culturing), the stiffness gradient of Ru-dECM changed from an initial range of 459 ± 92 to 20 ± 7 kPa in cell free Ru-dECM to 323 ± 97 to 22 ± 3 kPa in cell encapsulated Ru-dECM, whereas the dECM hydrogel's stiffness changed from approximately 8 ± 2 kPa in the absence of cells to about 6 ± 2 kPa in the presence of encapsulated cells (Fig. 3A). This observed small decrease in the stiffness gradient range was due to the fact that after cells were encapsulated in the hydrogel, the cells (as added elements in the hydrogel) also contributed to the overall stiffness. The stiffnesses of zones 2, 5, and 8, which represented high stiffness, medium stiffness and low stiffness, were 254 kPa, 120 kPa, and 31 kPa respectively after encapsulating the cells for 4 h. After 5 d, the gradient stiffness range was still maintained in the cell-free Ru-dECM hydrogel (Figure S2). A reduction in the magnitude of the stiffness occurred due to the swelling of the hydrogel under medium immersion (stiffness of cell-free Ru-dECM at 4 h ranged from 459 ± 92 kPa to 20 ± 7 kPa and changed to 269 ± 66 kPa to 11 ± 4 kPa at 5 d; The stiffness of cell-free dECM remained constant, with a stiffness of 8 ± 2 kPa at 4 h to 8 ± 2 kPa at 5 d (Figure S2)). Intriguingly, the stiffness gradient of cell-encapsulated Ru-dECM had vanished after 5d especially within the high stiffness part and the previously observed significant difference of stiffness between Ru-dECM and dECM at 4 h was no longer present by day 5 (Fig. 3A). The stiffness values of cell- encapsulated Ru-dECM at 5 d spanned from 27 ± 19 kPa to 3 ± 1 kPa and hovered at 4 ± 0.1 kPa for dECM.

Both Ru-dECM and dECM, when loaded with cells, retained their stress relaxation profiles, exceeding 87 % relaxation across all assessed durations, mirroring the cell-free hydrogels (Fig. 3B). The relaxation rate (time to reach 50 % stress relaxation) in cell encapsulated Ru-dECM hydrogel after 5d culture remained consistent at approximately 0.5 s. In contrast, the cell encapsulated dECM

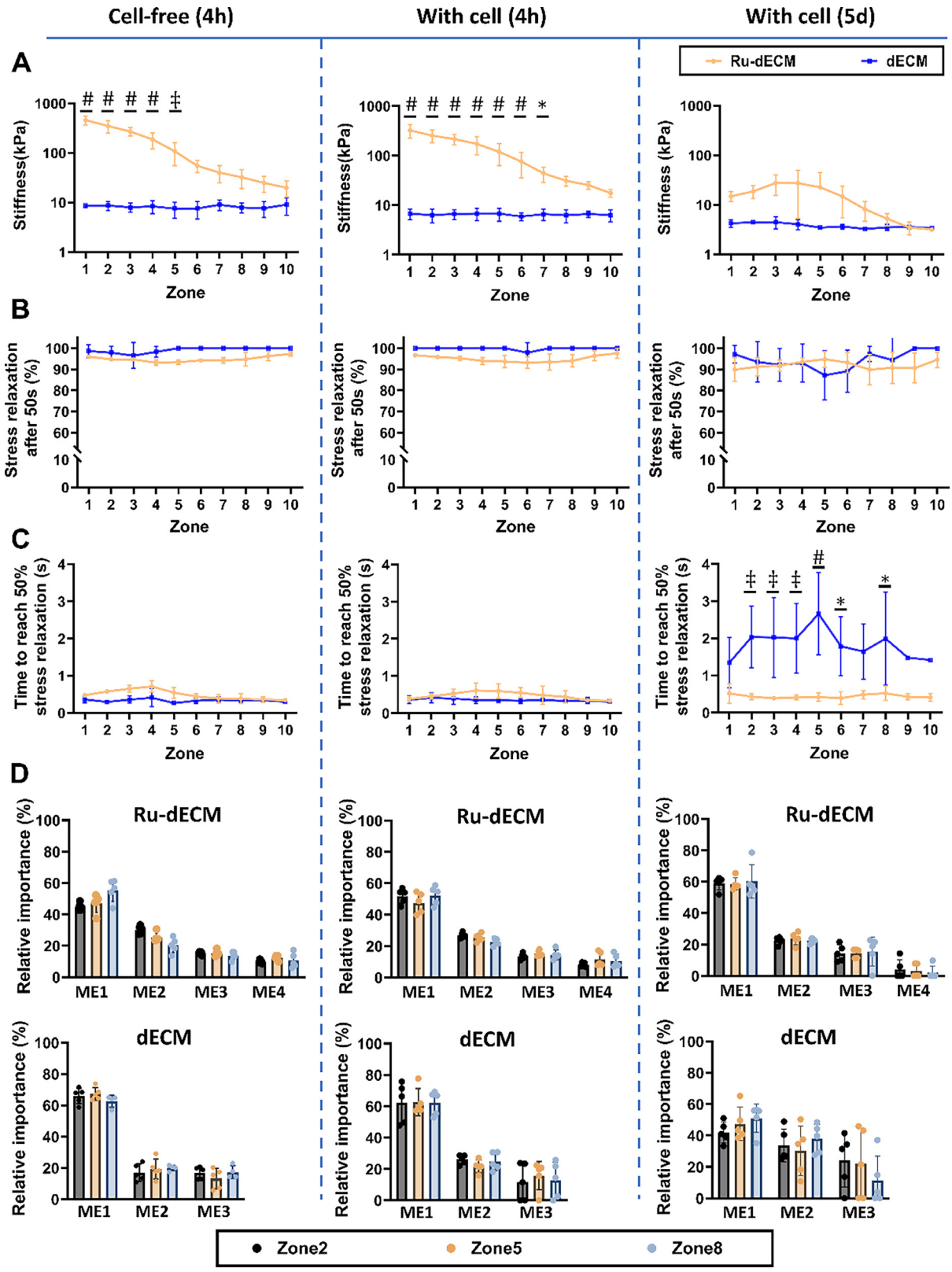

Fig. 3. Mechanical properties of both Ru-dECM and dECM hydrogels with and without encapsulated human dermal neonatal fibroblasts (HDFn) at 4 h and 5 d A) The stiffness of Ru-dECM and dECM hydrogels. B) Average stress relaxation behavior over 50 s duration. After compressing hydrogels using LLCT with a fixed 20 % strain ratio, the stress relaxation behavior was recorded over 50 s period. C) Time taken to reach 50 % stress relaxation. D) Analysis of the stress relaxation behavior through the generalized Maxwell model system. The relaxation profiles of both types of hydrogels with and without encapsulated cells over 50 s period was mathematically modelled using a Maxwell model system and the contribution (relative importance R_i) of each Maxwell element to the total relaxation was determined. For panel A, B and C, each dot represents the mean ± standard deviation generated from measurements on five independent hydrogels ($n = 5$). For panel D, each dot represents the measurement from each of five independent hydrogels ($n = 5$). Statistical significance was analyzed by two-way ANOVA with post hoc testing comparing each zone of Ru-dECM hydrogels with the corresponding zone of dECM hydrogels. (*, $p < 0.05$; ‡, $p < 0.01$; †, $p < 0.001$; #, $p < 0.0001$.).

Table 1
Relaxation time constants (τ) in seconds (s) of each Maxwell element for both Ru-dECM and dECM hydrogels with and without encapsulated cells. Zones 2, 5 and 8 correspond to high, medium and low stiffness regions on the gradient hydrogel.

		Ru-dECM				dECM			
Timepoint		τ_1	τ_2	τ_3	τ_4	τ_1	τ_3	τ_3	τ_4
4 h	zone2	0.3	1.3	6.5	75.4	0.2	1.6	17.1	–
Cell free	zone5	0.2	1.4	7.1	71.3	0.2	2.2	22.1	–
	zone8	0.2	1.2	6.3	64.9	0.3	2.4	8.5	–
	Average	**0.2 ± 0.03**	**1.3 ± 0.1**	**6.6 ± 0.4**	**71 ± 5**	**0.2 ± 0.04**	**2.1 ± 0.4**	**16 ± 7**	–
4 h	zone2	0.3	1.3	6.4	69.0	0.3	2.8	13.5	–
With cells	zone5	0.3	1.4	7.0	71.6	0.3	2.2	12.0	–
	zone8	0.2	1.3	7.2	81.2	0.2	1.9	9.6	–
	Average	**0.2 ± 0.03**	**1.3 ± 0.1**	**6.8 ± 0.4**	**74 ± 6**	**0.3 ± 0.02**	**2.2 ± 0.5**	**12 ± 2**	–
5 d	zone2	0.3	2.0	48.0	193.8	0.4	7.0	31.9	–
With cells	zone5	0.3	2.1	34.0	122.2	0.7	9.7	56.5	–
	zone8	0.3	3.8	76.8	108.6	0.8	10.7	47.2	–
	Average	**0.3 ± 0.03**	**2.6 ± 0.9**	**53 ± 22**	**142 ± 45**	**0.6 ± 0.2**	**9.1 ± 1.9**	**45 ± 12**	**–**

hydrogel had a protracted relaxation time (lower relaxation rate) at day 5 (τ∼2.0 s) compared to that at 4 h (τ∼0.5 s) (Fig. 3C). The requisite number of MEs remained unaltered after 5d for both cell encapsulated and unencapsulated hydrogels; three elements for dECM and four for Ru-dECM (Table 1 and Fig. 3D). After 4 h culture, the time constants *(τ)* of the MEs closely reflected those in cell-free hydrogels, shown by τ_1 0.2 s, τ_2 1.3 s and τ_3 6.8 s, with unique element 4 for τ_4 74 s in Ru-dECM and τ_1 0.3 s, τ_2 2.2 s and τ_3 12 s in dECM (Table 1). The relative importance corresponding to each element had not changed after 4 h cell encapsulation. After 5 d culture, although the presence of cells did not affect the number of ME, the characteristics of the MEs changed significantly compared to the initial 4 h stage (Fig. 3D). The τ values expanded for each element, with $\tau_1 \leq 1$ s, $1 < \tau_2 \leq 10$ s, $10 < \tau_3 \leq 60$ s, and the fourth element was $60 < \tau_4 \leq 150$ s (Table 1). Concurrently, alterations in the *Ri* of elements within both hydrogels were noted, displaying an increase in ME1 and a decrease for ME4 for Ru-dECM hydrogel, while there was a decrease in ME1 and an increase in ME2 & ME3 for dECM hydrogel.

3.4. Stiffness gradient does not affect the viability, migration and proliferation of HDFn, but causes changes in cell morphology and orientation

At all time points at least 85 % of the encapsulated fibroblasts were alive irrespective of the hydrogel crosslinking. Encapsulated cells (4 h) appeared rounded but had adopted a more stretched morphology after 1 d of culture (Fig. 4). This spindle-shaped morphology remained in both groups after 5 d culture albeit that fibroblasts tended to spread randomly in soft control gels, while these elongated more in a single direction in Ru-dECM gels. Cell spreading area and aspect ratio analyses revealed distinct morphological preferences of fibroblasts encapsulated within hydrogels over a one-day period (Figure S4). Notably, cells exhibited a pronounced spindle-shaped morphology with an aspect ratio of 2.0 in the soft dECM gel, while within the gradient stiffness of Ru-dECM, the aspect ratio of cells gradually increased as stiffness decreased, transitioning from 1.4 in zone 2 to 2.0 in zone 8 meaning that stiffness inhibited cell stretching. By day 5, the Ru-dECM induced elongation of fibroblasts up to an aspect ratio of 3.9 in all zone 2, 5 and 8, contrasting with the 2.9 aspect ratio observed in the soft dECM gel in which fibroblasts also had continued to stretch (Figure S4). While cell area increased with extended culture time, it remained unaffected by variations in mechanical cues and changes in cell shape. In control gels, cell densities appeared higher than in Ru-crosslinked gels. Yet, this related to the approximately 50% size reduction of the dECM hydrogel area (Figure S5).

We quantified the angular arrangement of the fibroblasts within the different hydrogels at 1 d and 5 d After 1 d the cells exhibited an orientation pattern within defined zones of the Ru-dECM hydrogel, with the degree of orientation appearing to be related to the stiffness range the cells experienced (Fig. 5B). More cells aligned between −80° to −30° relative to the stress axis (stiff to soft) in zone 5 and −60° to −30° in zone 8. This arrangement did not appear in zone 2 which was the region with the high stiffness (∼254 kPa). As we reported in the previous section: the fibroblasts cultured in 3D in the Ru-dECM hydrogel remodeled the hydrogel during the 5 d of culture to modulate the stiffness to decrease it within the initially high stiffness zones significantly to achieve a stiffness range between 27.2 to 3.2 kPa across the breadth of the hydrogel. In apparent response to these changes in mechanics, on the fifth day, the fibroblasts that had previously experienced a gradient stiffness in their environment in the Ru-dECM hydrogel all adopted a uniform cell orientation at an approximately −45° angular orientation to the gradient axis (stiff to soft) (Figure5). To represent the three-dimensional arrangement of cells in the hydrogel, the length (10 mm), width (8 mm), and height (1.5 mm) of the hydrogel were defined as the X, Y, and Z axes, respectively. Obviously, the x-axis is the gradient axis where the stiffness gradient exists. The cell directional alignment was found to only occur in the XY-plane rather than along the Z-axis. In contrast, in control dECM gels the cells maintained their random orientation throughout the culture period.

Ki67 immunofluorescence staining showed that the stiffness gradient did not affect the proliferation of fibroblasts. The proliferation indexes of HDFn (percentage of Ki67 positive cells) cultured in Ru-dECM and dECM were less than 10% after 1 d and 5 d (Figure S6). There was also no difference in the number of proliferating cells in each zone in any of the hydrogels regardless of the time in culture. In addition, there were no differences in the number of cells in each zone in any of the hydrogels (Figure S6C). The uniform distribution of cell numbers throughout the gradient stiffness hydrogel may suggest the absence of cell migration (prominent durotaxis) under the conditions of our experiment. However, this was an indirect observation, and further investigation would be required to substantiate this observation.

3.5. The ECM fiber structure observation in no cell-encapsulated dECM and Ru-dECM hydrogels

The ultrastructure of the hydrogel was visualized by SEM (Figure. S7A) at 25,000x magnification. Irrespective of the Ru-crosslinking, the skin-derived ECM hydrogels comprised a network

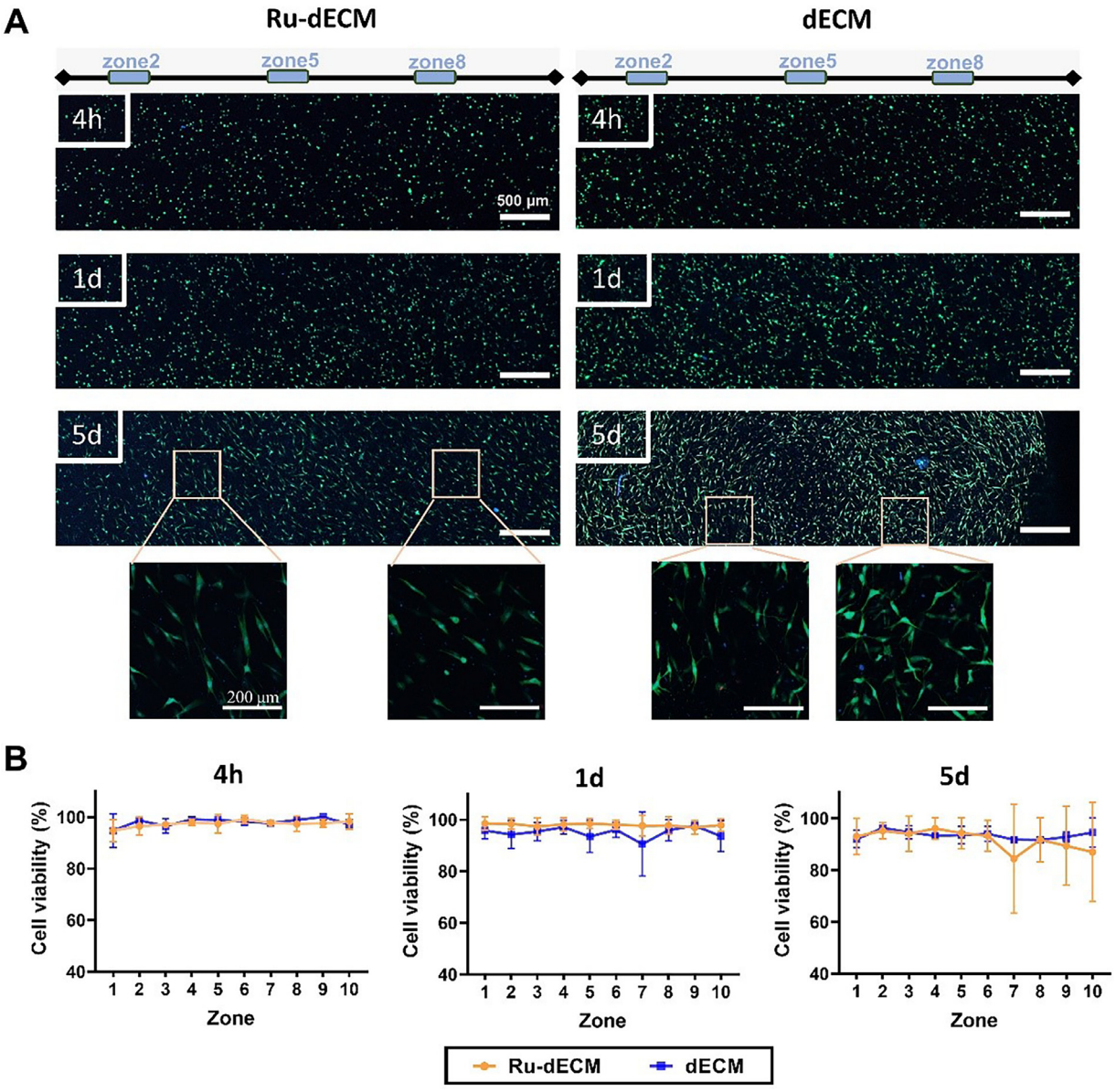

Fig. 4. Live/dead staining on HDFn fibroblasts encapsulated in Ru-dECM and dECM hydrogels at 4 h, 1 d and 5 d A) Cells were stained with Calcein AM (green) for living cells, propidium iodide (red) for dead cells and Hoechst (blue) for cell nuclei. Scale bars depict 500 μm. B) Cell viability percentage was calculated based on Fiji quantification of fluorescently labelled cells. Each dot represents the mean ± standard deviation generated from three independent hydrogels testing ($n = 3$). Statistical significance was analyzed by two-way ANOVA with post hoc testing comparing each zone of Ru-dECM hydrogels with the corresponding zone of dECM hydrogels. (ns or unmarked, not significant).

of randomly organized fibers, with the fibers showing a striped repeat pattern typical for collagen fibers. However, the arrangement of fibers in Ru-dECM was denser than that in dECM, especially in zone2 of Ru-dECM. Moreover, the diameter of the fibers in zone2 of Ru-dECM were significantly greater than that in zone5 of Ru-dECM and the control dECM. The 'percentage of pores' corresponds to the proportion of pore area relative to the entire image. While the number of pores in the RuECM hydrogel did not differ from control dECM hydrogel (Figure S7C), Ru crosslinking reduced the fraction of mesh holes compared to control dECM gel (Ru-dECM zone2: 0.33 ± 0.09; Ru-dECM zone5: 0.42 ± 0.04; Ru-dECM zone8: 0.50 ± 0.03; dECM: 0.50 ± 0.003 (Figure S7D). In contrast, Ru crosslinking in hydrogels had no influence on the intersection density (the intersection number per μm^2). (Figure S7E)."

3.6. Time-dependent matrix fiber remodeling in cell-encapsulated dECM and Ru-dECM hydrogels

Cells encapsulated in the hydrogels, altered collagen architecture and increased the fiber density in Ru-dECM hydrogels compared to those in the dECM hydrogels (Fig. 6A). The increase in collagen fiber density was stiffness dependent in the Ru-dECM hydrogels. The PSR stained collagen fibers for dECM hydrogel at 4 h appeared diffused and homogeneously dense in all zones. In contrast, the fiber density for the Ru-dECM at 4 h was greater in the vicinity of zone 1 and lower near the softer end of the gradient i.e. zone 10. This was also evident from the mean fluorescence intensity (MFI) of collagen fibers per unit area which was determined using Fiji (Fig. 6B). Ru-induced crosslinking increased the MFI in the cell-loaded Ru-dECM hydrogel, where the MFI in the softest

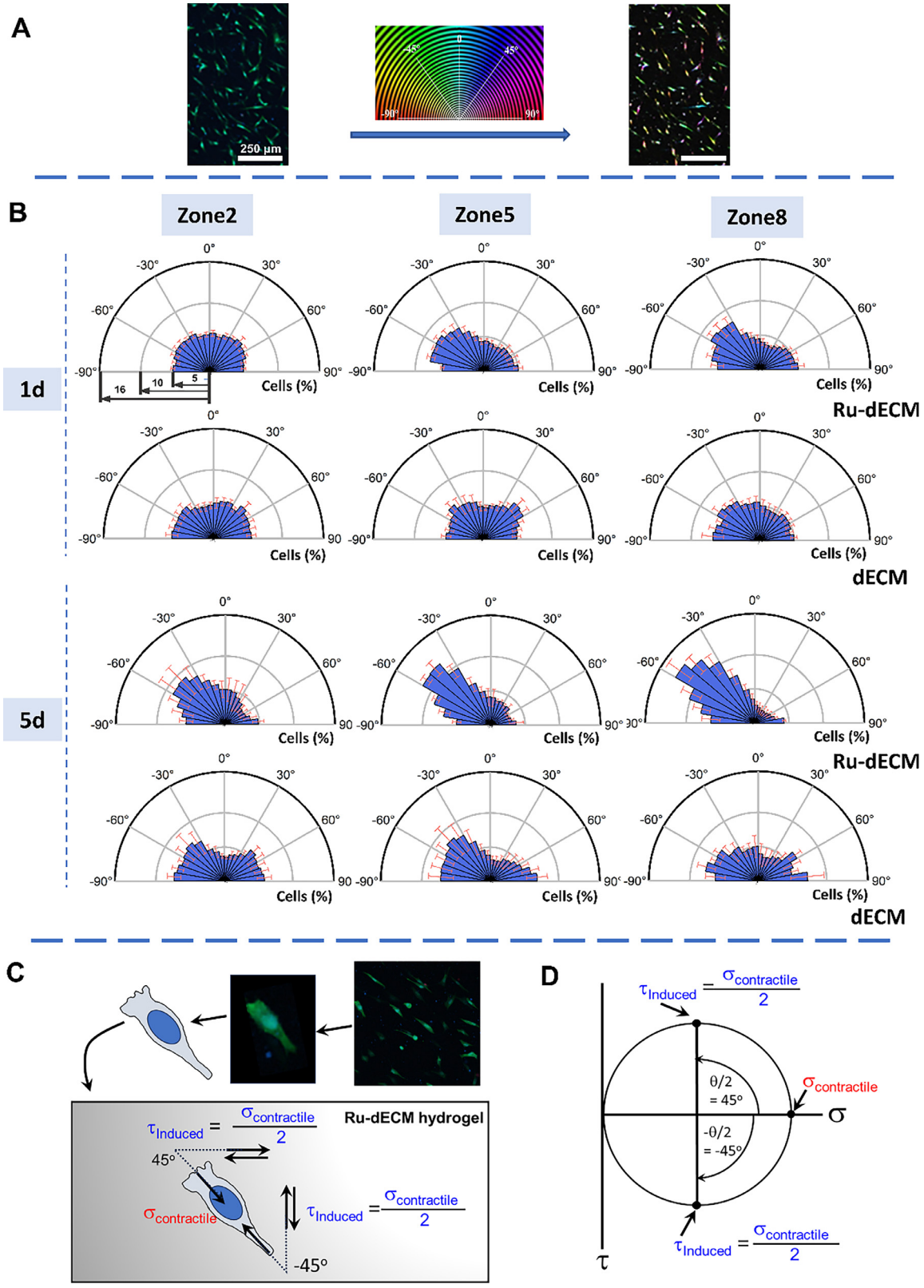

Fig. 5. Distribution of HDFn cells orientation in Ru-dECM and dECM hydrogels after 5 d A) Orientation J software package as the plugin for Fiji was used to evaluate the orientation of HDFn cells generating a visual representation of the orientation based on the circular hue, saturation and brightness (HSB) color map coding. The left panel is a representative fluorescence micrograph of HDFn cells in zone 5 of Ru-dECM hydrogel stained for living cells (Calcein AM (green)), dead cells (propidium iodide (red)) and cell nuclei (Hoechst (blue)); the middle panel is the circular HSB color map coding; and the right panel is the color-coded orientation survey for the HDFn cells in zone 5. Scale bar: 250 μm. B) Orientation distributions of HDFn cells in zones 2, 5 and 8 in Ru-dECM and dECM hydrogels after 1 d and 5 d. C) A 2D schematic showing that cells maximized the induced shear stress on the hydrogel along and across to the gradient by aligning themselves 45° to the long axis. D) A plain strain Mohr's circle showing how the contractile normal stresses imposed by the cells transform and induce maximum possible shear stresses on the hydrogel along and across the long axis with a magnitude of half of the contractile normal stresses.

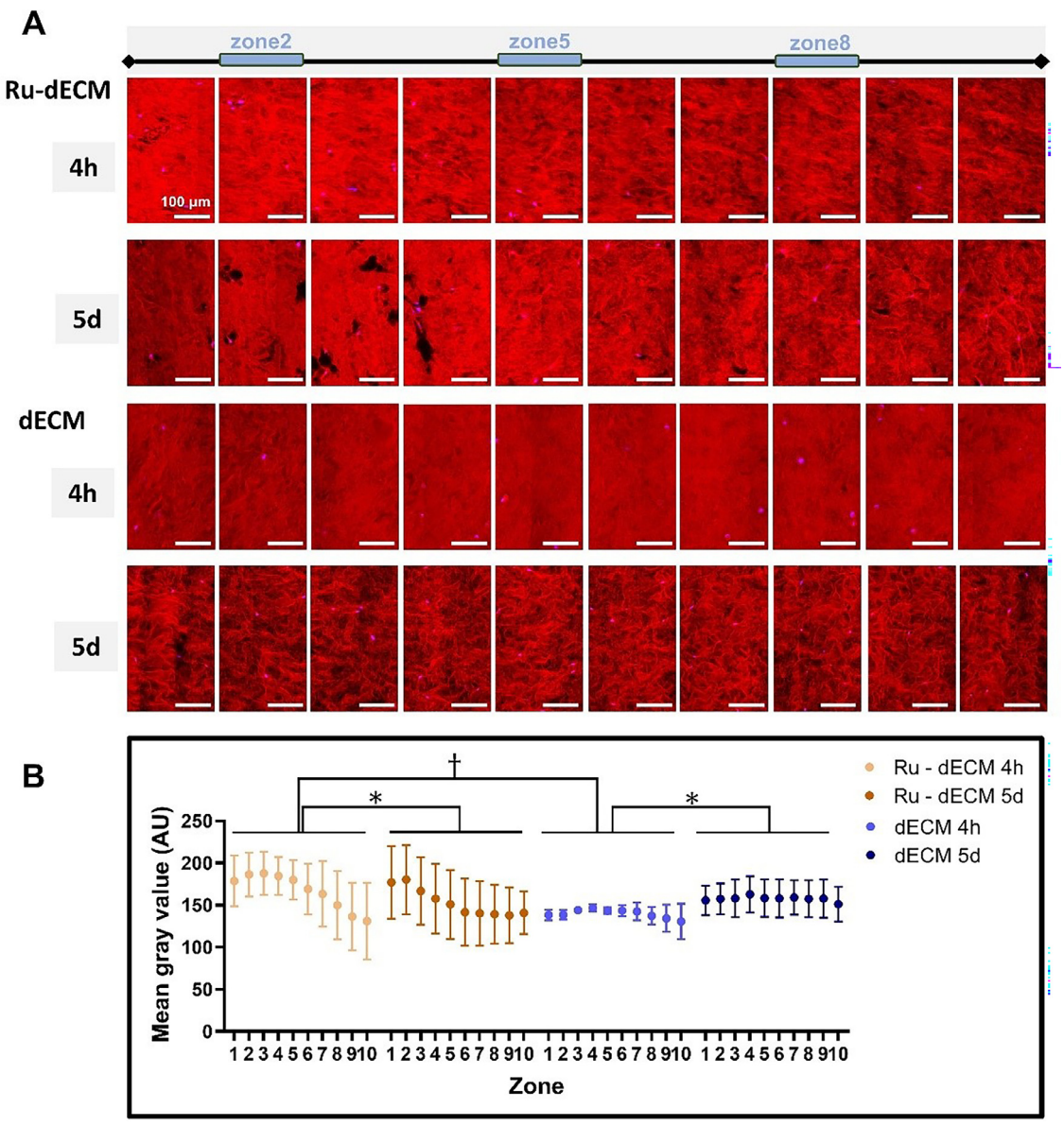

Fig. 6. Picrosirius red staining on Ru-dECM and dECM hydrogel slices and fiber characteristics analysis on the collagen network. Ru-dECM and dECM hydrogel slices were stained using Picrosirius red (PSR) staining and generated fluorescent images were analyzed using Fiji. A) Representative images of PSR staining on Ru-dECM and dECM hydrogel slices after 4 h and 5 d cell culturing. (cell nuclei-blue (Hoechst); collagen fiber-red (PSR)) Scale bars: 100 μm. B) Quantification for fiber Mean grey value (Integrated Density/Area, Integrated Density: the sum of the fluorescent signal of pixels of all collagen fibers in an area) for 10 zones in Ru-dECM and dECM hydrogels. Each dot represents the mean ± standard deviation generated from measurements on five independent hydrogels ($n = 5$). Statistical significance was analyzed by one-way ANOVA through comparing the area below the curve data (*, $p < 0.05$; †, $p < 0.001$).

part (zone 10) of Ru-dECM at 4 h was similar to that in control dECM hydrogel (Fig. 6B), while the intensity of the collagen fiber fluorescence signal increased towards zone 1.

The striking feature in the Ru-dECM hydrogel after 5 d of cell culture was the appearance of voids (pores) within the collagen network in zones 1–4 and the decreased MFI in zone 3 - 8 compared to 4 h (Fig. 6B). The fiber intensity in the softest part (zone 10) of Ru-dECM hydrogel was similar to that observed in control dECM hydrogel, showing the formation of defined interlaced collagen fiber bundles (Fig. 6A) and the increased MFI (Fig. 6B).

In detailed view, the collagen fibers surrounding fibroblasts in zones 2, 5, and 8 after 5 days, showed the fibers had been reorganized compared to freshly encapsulated (4 h) fibroblasts (Figure S8). In zone 2 (high stiffness) of Ru-dECM, larger pores had appeared in the immediate vicinity of encapsulated fibroblasts. This suggested that fibroblasts had degraded the collagen and /or rearranged the collagen fibers' assembly pattern through exertion of pulling/pushing forces upon the fibers or both. Within zones 5 and 8 (medium and low stiffness) of Ru-dECM respectively, the fibroblasts demonstrated interconnectivity with the surrounding fibers and there were no pores in the collagen fiber network appearing around the cells. In dECM hydrogels, the pattern of fiber bundle assembly in the matrix surrounding the cells was clearly visible. (Figure S8).

4. Discussion

The biomechanical dynamics of scar tissue formation after skin injury has been a focus of interest in histopathology and regenerative medicine. Our goal was to construct an *in vitro* model to elucidate the responses of dermal fibroblasts to a stiffness gradient. A major outcome of this study was the establishment of a versatile skin-derived ECM hydrogel platform with gradient stiffness starting at ~20 kPa and enabling a 23-fold log linear in-

crease over 5 mm generated using Ruthenium diffusion and UV/vis crosslinking. The Ru-dECM hydrogel exhibited stress relaxation behavior which required an extra ME to describe the relaxation pattern over the 3 required for the dECM hydrogel. Coinciding with the increasing gradient of stiffness, the collagen fiber density also increased. Furthermore, encapsulated fibroblasts re-oriented from a random alignment to 45° angle relative to the direction of the gradient stiffness that was present when the hydrogels were established with Ru-dECM, but not in dECM, after 5 d Finally, the fibroblasts remodeled their surrounding matrix to reach their optimal conditions, regardless of the initial stiffness in their environment. Regarding mechanical changes, the fibroblast activity over the 5 d caused the disappearance of the gradient stiffness of Ru-dECM, the extension of the ME time constants (τ) both in Ru-dECM and dECM hydrogels (Fig. 3D, Tables 1 and S1) and the decrease in relaxation rate in cell-encapsulated dECM gels after 5 d.

Our model provides an ideal platform for *in vitro* reconstruction of the physiological stiffness of normal skin and scars. In our model, the stiffness obtained in dECM hydrogel (8 ± 2 kPa) was comparable to the normal dermis (12 ± 4 kPa, Figure S3). In fibrotic skin the stiffness was observed to increase up to 20-fold compared to healthy skin dermis and in our Ru-dECM model we were able to achieve a 23-fold increase at the stiff end as compared to the soft end of our hydrogel [45,46]. Recently, a series of physically/photopolymerized cross-linked hydrogels have been used to systematically investigate the effects of gradient stiffness substrates on cell behavior [47]. However, these studies primarily focused on a single natural polymer such as hyaluronic acid or synthetic hydrogels such as polyacrylic acid and their effects on cell behavior in 2D. Notably, our skin-derived gradient stiffness hydrogels and encapsulated fibroblast 3D cultures were developed to be the first system that can replicate the natural biochemical environment of cells in terms of composition, structure, and dimensions. Furthermore, our strategy of Ru diffusion and UV/vis crosslinking can potentially be utilized to model other fibrotic tissues (e.g., pulmonary fibrosis, cirrhosis) and assess their related cellular responses, using the respective organ derived ECMs.

Ruthenium crosslinking depends on the covalent chemical crosslinking formed between tyrosines, known as di-tyrosine bonds [48]. It is noteworthy that the Ru-induced covalent bonds within the hydrogels introduced an additional Maxwell element-ME4 (which had the longest relaxation time constant), which was necessary when fitting the relaxation curve description and was accompanied by the redistributed relative importance of each ME. Typically, ME1, which is usually of the highest relative importance, can be attributed to the redistribution of the most abundant and fastest-moving free water molecules in the hydrogel. Other MEs may correspond to small molecules, cells, or types of crosslinks formed in the ECM [49]. However, compared to skin tissue, both hydrogels exhibited significantly higher total stress relaxation percentage in 50 s and a faster initial relaxation rate. This aligns with a previous study, where a dECM hydrogel derived from human lung tissue displayed a higher total relaxation than its derivative tissue [50], likely due to the complete removal of cells, reconfiguration of ECM proteins and the (partial) disruption of chemical crosslinks during decellularization.

Additionally, SEM images showed that the ECM structure comprised of randomly organized fibers both in non-crosslinked and crosslinked hydrogels. However, crosslinking had caused a decreased porosity, and simultaneously increased the fiber diameter due to an increase of the tight connections between fibrils. Moreover, the observed changes in collagen fiber density of cell-encapsulated Ru-dECM (4 h) directly correlated with the degree of crosslinking, consistent with our prior research of lung-derived dECM hydrogels in which crosslinking resulted in a denser collagen matrix with decreased fiber lengths [36]. The notable density increase of collagen fibers at the stiffer end of the Ru-dECM mirrors the highly crosslinked outcome of scar ECM *in vivo*, providing an optimal environment for studying how fibroblasts inherently respond to increases in matrix stiffness and crosslinking.

Matrix stiffness directs the morphology and migration of fibroblasts [51,52]. Different from 2D where increased adhesion, proliferation, average cell area and aspect ratio of fibroblasts have been observed towards the stiffer end of surfaces [25], the fibroblasts cultured in the 3D stiffness gradient only exhibited a high aspect ratio (∼3.9) and an oriented arrangement (∼ −45° angular orientation) after 5d while there were no significant changes in cell spreading area, cell proliferation and migration. Our data strongly suggest that the prior experience of a stiffness gradient is an essential requirement to motivate cell alignment, because no cell alignment was observed in the dECM hydrogels. This observation is consistent with studies that indicate cell morphology and orientation are influenced by the steepness (slope) of the gradient [53,54]. Furthermore, a relatively low stiffness (≤ 120 kPa) environment is necessary for enabling cell alignment: this can be observed in Fig. 5B where at day 1 the cell alignment is only observed for zones 5 and 8 with stiffnesses ≤ 120 kPa. In zone 2 alignment was only observed at day 5 when the stiffness had been reduced below 120 kPa by the cellular activities (Fig. 5B).

To our knowledge we are the first to observe this stiffness gradient induced cell alignment in 3D cultures. Fibroblasts sensed the stimulation of the stiffness gradient and exerted tension on the surrounding ECM to achieve orientation. High stiffness is driving encapsulated fibroblasts to remodeling i.e. reduce stiffness. Below a threshold stiffness, fibroblasts that had previously experienced the gradient, gain the ability to align to the longitudinal (gradient) axis of the hydrogel. Since we did not observe preferred alignment of the collagen fibers the reasons for cell alignment could be related to generation of internal stresses in the hydrogel caused by cellular contractile forces. The cellular contractile force in dECM hydrogel caused shrinkage of the hydrogels at day 5 (Figure S5), akin to the contracture observed in dermal scar tissue. Ru-dECM hydrogels, on the other hand, resisted shrinking by opposing the cellular contractile forces through the Ru induced covalent bonds in their matrix network [55,56]. Alignment of cells to 45° could possibly be interpreted as an effort by the cells to maximize the leverage of their longitudinal contractile normal stress ($\sigma_{\text{contractile}}$) on the 3D shear stresses (τ_{induced}) necessary for hydrogel shrinking, which now occurs along and across the long axis of the Ru-dECM hydrogel (Fig. 5C and D) [57].

The cells orientated randomly in the dECM non-covalently bonded hydrogels and these hydrogels contract because the contractile stresses applied by the cells individually to their local environment are collectively enough to overcome the resistance to shrinkage. Therefore, there is no reason for these cells to change their orientation. However, for cells in the RuECM crosslinked hydrogel the covalent bonded matrix offered additional resistance to shrinkage thus the cells needed to align themselves in an orientation where the effect of their individual contractile forces is maximized and could challenge the resistance offered by the hydrogel.

A solid metal or ceramic object is composed of interconnected (bonded via metallic, covalent or ionic bonds) atoms or molecules, similarly a plastic material or hydrogel is composed of interconnected (through physical interactions or covalent bonds) polymers. As a consequence to external or internal stresses the solid objects deform, which is measured in terms of strain (e.g. shrinkage of dECM gels). Only, two type of stresses can exist in a solid object namely, normal (pulling/pushing) or shear (sliding) stress. The interconnections in solid objects cause the normal stresses active in one direction to transform and manifest themselves on other direction as shear stresses or vice versa. This phenomenon of stress transformation in 2D is visualized through the Mohr's circle [58] as

depicted in Fig. 5D which shows that if normal contractile stresses pull on the hydrogel then at 45° orientation these normal stresses transform and induce a certain maximum shear stresses and this happens along and across the hydrogel if all the cells align themselves 45° to the longitudinal (gradient) hydrogel axis.

Changes in cell alignment were driven by mechano-transduction signaling in the fibroblasts. Mechanical cues from the surrounding matrix also cause fibroblasts to induce matrix remodeling and regulation of mechanical properties [7,59]. Our results showed that fibroblast-mediated ECM remodeling is governed by the stiffness value of the cell-surrounding ECM. The Ru-crosslinking at the stiffer end of the gradient resulted in a denser collagen network structure (seen at 4 h), which, in the presence of fibroblasts, underwent specific remodeling of the cell surrounding matrix to reach the optimal conditions for the fibroblasts over an extended culture time (5 d). After 5d, the fibroblasts degraded collagen and/or re-assembled collagen fibers to induce a decrease in stiffness at the stiffest regions of Ru-dECM. In addition, the fibroblasts rearranged the random ECM matrix into dense fiber bundles over short ranges in the softest part i.e. zone 10 of Ru-dECM and whole of dECM, which is consistent with the typical basket-weave structure that exists in normal dermal tissue [26]. Interestingly, fibroblasts also modulated the viscoelasticity of dECM hydrogels by slowing down the rate of stress relaxation both for dECM and Ru-dECM hydrogels (Table S1) accompanied by a redistribution of the relative importance of individual MEs, which we hypothesize is related to the increased collagen intermolecular forces in the hydrogel and the resulting increased plasticity.

4. Conclusion

In conclusion, Ruthenium diffusion followed by UV/vis crosslinking of skin-derived ECM gave rise to a stiffness gradient Ru-dECM hydrogel with a 23-fold increase in stiffness. This hydrogel provides a promising *in vitro* 3D model for elucidating fibroblast responses to stiffness gradients seen in scar transitions. The findings in this study suggest the stiffness gradient within the *in vitro* scar model directs fibroblast's alignment in regions below 120 kPa stiffness. Fibroblasts remodel the matrix within their vicinity in regions with stiffness higher than 120 kPa causing a decrease in stiffness. Overall, this study adds to understanding of how the mechanics of fibrosis affects resident fibroblasts. This model can be further extended to *in vitro* engineering of different tissues such as heart and liver and used as a platform for fibrotic disease modeling studies in different tissue systems. However, as our platform is a model it will not fully capture the complexity of *in vivo* scar formation and remodeling processes. Our platform, however, does allow to dissect the interaction between tissue fibroblasts and tissue-derived ECM as a function of a stiffness gradient. Scar tissue stiffness can vary significantly due to factors such as the age of the scar and individual healing responses. We plan to explore these aspects in future work, seeking to better understand the nuances of tissue stiffness gradients, fibroblast behavior, and scar formation in the context of wound healing and tissue engineering.

Declaration of competing interest

The authors declare that they have no known competing financial interests or personal relationships that could have appeared to influence the work reported in this paper.

CRediT authorship contribution statement

Fenghua Zhao: Conceptualization, Investigation, Methodology, Visualization, Writing – original draft. **Meng Zhang:** Investigation, Methodology. **Mehmet Nizamoglu:** Investigation, Methodology. **Hans J. Kaper:** Investigation, Methodology. **Linda A. Brouwer:** Investigation, Methodology. **Theo Borghuis:** Investigation, Methodology. **Janette K. Burgess:** Conceptualization, Data curation, Writing – review & editing. **Martin C. Harmsen:** Conceptualization, Formal analysis, Supervision, Visualization, Writing – review & editing. **Prashant K. Sharma:** Conceptualization, Data curation, Writing – review & editing.

Acknowledgements

Part of the work has been performed at the UMCG Imaging and Microscopy Center (UMIC), which is sponsored by NWO (Dutch Research Council)-grant 175-010-2009-023. The authors thank Klaas Sjollema for the assistance with utilization of microscopes at UMIC. The authors would like to thanks China Scholarship Council and the GSMS in the University of Groningen for the financial support to FZ (Grant No. 202006240071). Nederlandse Organisatie voor Wetenschappelijk Onderzoek (NWO) Aspasia-premie subsidienummer 015.013.010 awarded to JKB.

Supplementary materials

Supplementary material associated with this article can be found, in the online version, at doi:10.1016/j.actbio.2024.05.018.

References

[1] J.F. Almine, S.G. Wise, A.S. Weiss, Elastin signaling in wound repair, Birth Defects Res. C 96 (3) (2012) 248–257.
[2] H. Sorg, D.J. Tilkorn, S. Hager, J. Hauser, U. Mirastschijski, Skin wound healing: an update on the current knowledge and concepts, Eur. Surg. Res. 58 (1–2) (2017) 81–94.
[3] A.F. Spielman, M.F. Griffin, J. Parker, A.C. Cotterell, D.C. Wan, M.T. Longaker, Beyond the scar: a basic science review of wound remodeling, Adv. Wound Care 12 (2) (2023) 57–67.
[4] J.M. Reinke, H. Sorg, Wound repair and regeneration, Eur. Surg. Res. 49 (1) (2012) 35–43.
[5] H.E. Talbott, S. Mascharak, M. Griffin, D.C. Wan, M.T. Longaker, Wound healing, fibroblast heterogeneity, and fibrosis, Cell Stem Cell 29 (8) (2022) 1161–1180.
[6] L. Moretti, J. Stalfort, T.H. Barker, D. Abebayehu, The interplay of fibroblasts, the extracellular matrix, and inflammation in scar formation, J. Biol. Chem. 298 (2) (2022) 101530.
[7] B. Li, J.H. Wang, Fibroblasts and myofibroblasts in wound healing: force generation and measurement, J. Tissue Viability. 20 (4) (2011) 108–120.
[8] L. Van De Water, S. Varney, J.J. Tomasek, Mechanoregulation of the myofibroblast in wound contraction, scarring, and fibrosis: opportunities for new therapeutic intervention, Adv. Wound Care 2 (4) (2013) 122–141.
[9] A.L. Rippa, E.P. Kalabusheva, E.A. Vorotelyak, Regeneration of dermis: scarring and cells involved, Cells 8 (6) (2019).
[10] D.G. Janson, G. Saintigny, A. van Adrichem, C. Mahe, A. El Ghalbzouri, Different gene expression patterns in human papillary and reticular fibroblasts, J. Invest. Dermatol. 132 (11) (2012) 2565–2572.
[11] A. Shpichka, D. Butnaru, E.A. Bezrukov, R.B. Sukhanov, A. Atala, V. Burdukovskii, Y. Zhang, P. Timashev, Skin tissue regeneration for burn injury, Stem Cell Res. Ther. 10 (1) (2019) 94.
[12] J.J. Tomasek, G. Gabbiani, B. Hinz, C. Chaponnier, R.A. Brown, Myofibroblasts and mechano-regulation of connective tissue remodelling, Nat. Rev. Mol. Cell Biol. 3 (5) (2002) 349–363.
[13] J. Godwin, D. Kuraitis, N. Rosenthal, Extracellular matrix considerations for scar-free repair and regeneration: insights from regenerative diversity among vertebrates, Int. J. Biochem. Cell Biol. 56 (2014) 47–55.
[14] T.R. Cox, J.T. Erler, Remodeling and homeostasis of the extracellular matrix: implications for fibrotic diseases and cancer, Dis. Model. Mech. 4 (2) (2011) 165–178.
[15] M. Xue, C.J. Jackson, Extracellular matrix reorganization during wound healing and its impact on abnormal scarring, Adv. Wound Care 4 (3) (2015) 119–136.
[16] S. Mueller, G. Millonig, L. Sarovska, S. Friedrich, F.M. Reimann, M. Pritsch, S. Eisele, F. Stickel, T. Longerich, P. Schirmacher, H.K. Seitz, Increased liver stiffness in alcoholic liver disease: differentiating fibrosis from steatohepatitis, World J. Gastroenterol. 16 (8) (2010) 966–972.
[17] T.J.H. Narasimham, L. Parinandi, Cardiovascular Signaling in Health and Disease, Springer, Cham (CH), 2022.
[18] J.K. Burgess, M.C. Harmsen, Chronic lung diseases: entangled in extracellular matrix, Eur. Respir. Rev. 31 (163) (2022).
[19] S. Rayego-Mateos, S. Campillo, R.R. Rodrigues-Diez, A. Tejera-Munoz, L. Marquez-Exposito, R. Goldschmeding, D. Rodriguez-Puyol, L. Calleros,

M. Ruiz-Ortega, Interplay between extracellular matrix components and cellular and molecular mechanisms in kidney fibrosis, Clin. Sci. 135 (16) (2021) 1999–2029.
[20] B.R. Seo, X. Chen, L. Ling, Y.H. Song, A.A. Shimpi, S. Choi, J. Gonzalez, J. Sapudom, K. Wang, R.C. Andresen Eguiluz, D. Gourdon, V.B. Shenoy, C. Fischbach, Collagen microarchitecture mechanically controls myofibroblast differentiation, Proc. Natl. Acad. Sci. U S A 117 (21) (2020) 11387–11398.
[21] T. Yeung, P.C. Georges, L.A. Flanagan, B. Marg, M. Ortiz, M. Funaki, N. Zahir, W. Ming, V. Weaver, P.A. Janmey, Effects of substrate stiffness on cell morphology, cytoskeletal structure, and adhesion, Cell Motil. Cytoskeleton 60 (1) (2005) 24–34.
[22] A. Jagiello, U. Castillo, E. Botvinick, Cell mediated remodeling of stiffness matched collagen and fibrin scaffolds, Sci. Rep. 12 (1) (2022) 11736.
[23] A. Wahlsten, D. Rutsche, M. Nanni, C. Giampietro, T. Biedermann, E. Reichmann, E. Mazza, Mechanical stimulation induces rapid fibroblast proliferation and accelerates the early maturation of human skin substitutes, Biomaterials 273 (2021) 120779.
[24] F. Feng, M. Liu, L. Pan, J. Wu, C. Wang, L. Yang, W. Liu, W. Xu, M. Lei, Biomechanical regulatory factors and therapeutic targets in keloid fibrosis, Front. Pharmacol. 13 (2022) 906212.
[25] I. Hopp, A. Michelmore, L.E. Smith, D.E. Robinson, A. Bachhuka, A. Mierczynska, K. Vasilev, The influence of substrate stiffness gradients on primary human dermal fibroblasts, Biomaterials 34 (21) (2013) 5070–5077.
[26] R.A. Brown, In the beginning there were soft collagen-cell gels: towards better 3D connective tissue models? Exp. Cell Res. 319 (16) (2013) 2460–2469.
[27] R.I. R.I, R. do Amaral, R.L. Reis, A.P. Marques, C.M. Murphy, F.J. O'Brien, 3D-Printed gelatin methacrylate scaffolds with controlled architecture and stiffness modulate the fibroblast phenotype towards dermal regeneration, Polymers 13 (15) (2021).
[28] C. Branco da Cunha, D.D. Klumpers, W.A. Li, S.T. Koshy, J.C. Weaver, O. Chaudhuri, P.L. Granja, D.J. Mooney, Influence of the stiffness of three-dimensional alginate/collagen-I interpenetrating networks on fibroblast biology, Biomaterials 35 (32) (2014) 8927–8936.
[29] Z. Zhao, G. Huang, Y. He, X. Zuo, W. Han, H. Li, Extracellular matrix stiffness regulates fibroblast differentiation by influencing DNA methyltransferase 1 expression through microtubule polymerization, bioRxiv. 10 (2022) 1101.
[30] N. Migulina, R.H.J. de Hilster, S. Bartel, R.H.J. Vedder, M. van den Berge, A. Nagelkerke, W. Timens, M.C. Harmsen, M.N. Hylkema, C.A. Brandsma, J.K. Burgess, 3-D culture of human lung fibroblasts decreases proliferative and increases extracellular matrix remodeling genes, Am. J. Physiol. Cell Physiol. 326 (1) (2024) C177–C193.
[31] S. Ishihara, H. Kurosawa, H. Haga, Stiffness-modulation of collagen gels by genipin-crosslinking for cell culture, Gels 9 (2) (2023).
[32] Y. Ren, H. Zhang, Y. Wang, B. Du, J. Yang, L. Liu, Q. Zhang, Hyaluronic acid hydrogel with adjustable stiffness for mesenchymal stem Cell 3D culture via related molecular mechanisms to maintain stemness and induce cartilage differentiation, ACS. Appl. Bio Mater. 4 (3) (2021) 2601–2613.
[33] Z. Shariatinia, A.M. Jalali, Chitosan-based hydrogels: preparation, properties and applications, Int. J. Biol. Macromol. 115 (2018) 194–220.
[34] Y. Liu, J. Mao, Z. Guo, Y. Hu, S. Wang, Polyvinyl alcohol/carboxymethyl chitosan hydrogel loaded with silver nanoparticles exhibited antibacterial and self-healing properties, Int. J. Biol. Macromol. 220 (2022) 211–222.
[35] Y. Liang, Y. Shen, X. Sun, H. Liang, Preparation of stretchable and self-healable dual ionically cross-linked hydrogel based on chitosan/polyacrylic acid with anti-freezing property for multi-model flexible sensing and detection, Int. J. Biol. Macromol. 193 (Pt A) (2021) 629–637.
[36] M. Nizamoglu, R.H.J. de Hilster, F. Zhao, P.K. Sharma, T. Borghuis, M.C. Harmsen, J.K. Burgess, An in vitro model of fibrosis using crosslinked native extracellular matrix-derived hydrogels to modulate biomechanics without changing composition, Acta Biomater. 147 (2022) 50–62.
[37] F.D. Martinez-Garcia, R.H.J. de Hilster, P.K. Sharma, T. Borghuis, M.N. Hylkema, J.K. Burgess, M.C. Harmsen, Architecture and composition dictate viscoelastic properties of organ-derived extracellular matrix hydrogels, Polymers 13 (18) (2021).
[38] M. Zhang, V.E. Getova, F.D. Martinez-Garcia, T. Borghuis, J.K. Burgess, M.C. Harmsen, From macro to micro: comparison of imaging techniques to detect vascular network formation in left ventricle decellularized extracellular matrix hydrogels, Gels. 8 (11) (2022).
[39] Z. Puspoki, M. Storath, D. Sage, M. Unser, Transforms and operators for directional bioimage analysis: a survey, Adv. Anat. Embryol. Cell Biol. 219 (2016) 69–93.
[40] I.Z.W. Chan, M. Stevens, P.A. Todd, D. Silvestro, pat-geom: a software package for the analysis of animal patterns, Methods Ecol. Evol. 10 (4) (2019) 591–600.
[41] N.A. Hotaling, K. Bharti, H. Kriel, C.G. Simon Jr., DiameterJ: a validated open source nanofiber diameter measurement tool, Biomaterials 61 (2015) 327–338.
[42] J. Schindelin, I. Arganda-Carreras, E. Frise, V. Kaynig, M. Longair, T. Pietzsch, S. Preibisch, C. Rueden, S. Saalfeld, B. Schmid, J.Y. Tinevez, D.J. White, V. Hartenstein, K. Eliceiri, P. Tomancak, A. Cardona, Fiji: an open-source platform for biological-image analysis, Nat. Methods 9 (7) (2012) 676–682.
[43] C. McQuin, A. Goodman, V. Chernyshev, L. Kamentsky, B.A. Cimini, K.W. Karhohs, M. Doan, L. Ding, S.M. Rafelski, D. Thirstrup, W. Wiegraebe, S. Singh, T. Becker, J.C. Caicedo, A.E. Carpenter, CellProfiler 3.0: next-generation image processing for biology, PLoS. Biol. 16 (7) (2018) e2005970.
[44] C.J. Morgan, Use of proper statistical techniques for research studies with small samples, Am. J. Physiol. Lung Cell Mol. Physiol. 313 (5) (2017) L873–L877.
[45] C. Huang, L. Liu, Z. You, B. Wang, Y. Du, R. Ogawa, Keloid progression: a stiffness gap hypothesis, Int. Wound J. 14 (5) (2017) 764–771.
[46] J.A. Clark, J.C.Y. Cheng, K.S. Leung, Mechanical properties of normal skin and hypertrophic scars, Burns 22 (6) (1996) 443–446.
[47] S.R. Polio, A.N. Kundu, C.E. Dougan, N.P. Birch, D.E. Aurian-Blajeni, J.D. Schiffman, A.J. Crosby, S.R. Peyton, Cross-platform mechanical characterization of lung tissue, PLoS ONE 13 (10) (2018) e0204765.
[48] H. Kim, B. Kang, X. Cui, S.H. Lee, K. Lee, D.W. Cho, W. Hwang, T.B.F. Woodfield, K.S. Lim, J. Jang, Light-activated decellularized extracellular matrix-based bioinks for volumetric tissue analogs at the centimeter scale, Adv. Funct. Mater. 31 (32) (2021).
[49] B.W. Peterson, H.C. van der Mei, J. Sjollema, H.J. Busscher, P.K. Sharma, A distinguishable role of eDNA in the viscoelastic relaxation of biofilms, mBio 4 (5) (2013) e00497-13.
[50] R.H.J. de Hilster, P.K. Sharma, M.R. Jonker, E.S. White, E.A. Gercama, M. Roobeek, W. Timens, M.C. Harmsen, M.N. Hylkema, J.K. Burgess, Human lung extracellular matrix hydrogels resemble the stiffness and viscoelasticity of native lung tissue, Am. J. Physiol. Lung Cell Mol. Physiol. 318 (4) (2020) L698–L704.
[51] S. Asano, S. Ito, K. Takahashi, K. Furuya, M. Kondo, M. Sokabe, Y. Hasegawa, Matrix stiffness regulates migration of human lung fibroblasts, Physiol. Rep. 5 (9) (2017).
[52] K.E.C. Blokland, M. Nizamoglu, H. Habibie, T. Borghuis, M. Schuliga, B.N. Melgert, D.A. Knight, C.A. Brandsma, S.D. Pouwels, J.K. Burgess, Substrate stiffness engineered to replicate disease conditions influence senescence and fibrotic responses in primary lung fibroblasts, Front. Pharmacol. 13 (2022) 989169.
[53] C. Kayal, E. Moeendarbary, R.J. Shipley, J.B. Phillips, Mechanical response of neural cells to physiologically relevant stiffness gradients, Adv. Healthc. Mater. 9 (8) (2020) e1901036.
[54] D. Joaquin, M. Grigola, G. Kwon, C. Blasius, Y. Han, D. Perlitz, J. Jiang, Y. Ziegler, A. Nardulli, K.J. Hsia, Cell migration and organization in three-dimensional in vitro culture driven by stiffness gradient, Biotechnol. Bioeng. 113 (11) (2016) 2496–2506.
[55] B.M. Baker, B. Trappmann, W.Y. Wang, M.S. Sakar, I.L. Kim, V.B. Shenoy, J.A. Burdick, C.S. Chen, Cell-mediated fibre recruitment drives extracellular matrix mechanosensing in engineered fibrillar microenvironments, Nat. Mater. 14 (12) (2015) 1262–1268.
[56] A. Lavrentieva, T. Fleischhammer, A. Enders, H. Pirmahboub, J. Bahnemann, I. Pepelanova, Fabrication of stiffness gradients of GelMA hydrogels using a 3D printed micromixer, Macromol. Biosci. 20 (7) (2020) e2000107.
[57] R.C. Hibbeler, Engineering Mechanics: Statics, SI Units, Pearson Education Limited, London, UK, 2022.
[58] F.P. Beer, R. E Jr., J.T. DeWolf, D.F. Mazurek, chapter 7.2: Mohr's Circle for Plane Stress, in: Mechanics of Materials-Seventh Edition, McGraw Hill, 2014, pp. 492–502.
[59] A.K. Schroer, W.D. Merryman, Mechanobiology of myofibroblast adhesion in fibrotic cardiac disease, J. Cell Sci. 128 (10) (2015) 1865–1875.